RSC Advances

PAPER

View Article Online
View Journal | View Issue

Cite this: *RSC Adv.*, 2024, **14**, 24092

Visible light driven (VLD) reduced TiO_{2-x} nanocatalysts designed by inorganic and organic reducing agent-mediated solvothermal methods for electrocatalytic and photocatalytic applications†

Sadaf Jamil, [a] Naila Jabeen,*[b] Fatima Sajid,[a] Latif U. Khan, [c] Afia Kanwal,[a] Manzar Sohail, [d] Muhammad Zaheer [e] and Zareen Akhter *[a]

This work presents a comparative study on the structural, optical and electrochemical characteristics of visible light driven (VLD) reduced titanium dioxide (TiO_{2-x}) nanocatalysts synthesized *via* inorganic and organic synthetic routes. X-ray diffraction (XRD) patterns, Raman spectra and X-ray absorption fine structure (XAFS) analyses reflected anatase phase titania. Whereas, the quantitative EXAFS fit and XANES analysis revealed structural distortion due to the presence of oxygen and titanium vacancies with low valent Ti states in anatase lattices of certain nanocatalysts, which subsequently leads to better electrochemical and photocatalytic activities. Moreover, owing to the large surface area and mesoporous structures, the Mg–TiO_{2-x} nanocatalysts exhibited enhanced water adsorption and ultimately increased overall water splitting with an OER overpotential equal to 420 mV *vs.* RHE at a current density of 10 mA cm^{-2} (Tafel slope = 62 mV dec^{-1}), extended visible light absorbance, decreased photoluminescence (PL) intensity and increased carrier lifetime in comparison with commercial titania.

Received 8th May 2024
Accepted 11th July 2024

DOI: 10.1039/d4ra03402c

rsc.li/rsc-advances

1. Introduction

In order to promote sustainable economic growth, it is increasingly crucial to maximize the efficiency of energy utilization and accelerate the adoption of renewable energy sources. One technology that can significantly contribute to the advancement of a sustainable energy system is water electrolysis. Basically, electrocatalytic water splitting involves the cathodic hydrogen evolution reaction (HER) and the anodic oxygen evolution reaction (OER). However, these reactions have been hampered by large overpotentials and sluggish kinetics.[1,2] Extensive studies have been conducted to investigate and develop non-precious transition metal oxide electrocatalysts that can be utilized efficiently in place of state of the art noble metal based (Ru, Ir, Pt) electrocatalysts for overall water splitting. Titanium oxide has garnered significant attention for environment[3] and green energy applications[4] owing to the high activity, non-toxicity, low cost, easy availability and chemical stability for pollutant degradation[5] and water splitting.[6] In addition, particle size, pore volume and surface area are found to be the key variables that influence the photocatalytic properties of titania.[7] However, low electrical conductivity,[8] unfavorable adsorption/desorption capability,[9] and large band gap (3.2 to 3.7 eV) of titania[10] limit its application in the environment and energy sector. In addition, sunlight contains a large proportion of visible light of which titania could utilize only <5% of the solar spectrum[10] which prevents titania showing efficient water splitting.

To overcome these limitations numerous efforts using different approaches have been adopted such as codoping,[11,12] introduction of intrinsic defects[13] and foreign species into the TiO_2 lattice,[14,15] crystal facet control[16] and the mesoporous structures architecture[17] *etc.* The morphological diversity and tunable conductivity span (semiconducting to metallic) are fascinating features of titania for enhancing optical and electrical properties. The main strategy behind these features is the defect generation that involves the optimization of conductivity, surface features, charge transport behavior and optical band gap energies of titania.[18] One way to modulate the electrocatalytic properties of TiO_2 nanocatalysts by using support

[a]*Department of Chemistry, Quaid-i-Azam University, Islamabad 45320, Pakistan*
[b]*Nanosciences and Technology Division, National Centre for Physics, QAU Campus, Shahdra Valley Road, P.O. Box 2141, Islamabad-44000, Pakistan. E-mail: Naila.jabeen@ncp.edu.pk; Naila.chem@gmail.com*
[c]*Synchrotron-light for Experimental Science and Applications in the Middle East (SESAME), P.O. Box 7, Allan 19252, Jordan*
[d]*School of Natural Sciences, National University of Sciences and Technology (NUST), H-12, Islamabad, Pakistan*
[e]*Lahore University of Management Sciences DHA, Lahore Cantt, 54792, Pakistan. E-mail: zareen_a@qau.edu.pk*

† Electronic supplementary information (ESI) available. See DOI: https://doi.org/10.1039/d4ra03402c

materials (Pd), with suitable facet exposed can give an additional adjusting path to regulate the HER activities of Pd–TiO_2 nanocatalysts.[19] Another technique for introducing lattice defects on pristine TNTs (titanium nanotubes) is ultrasonication method. This single-atom catalysts (SACs) create triggered chemical traps provides a pathway for controllable assembling stable and highly active single-atomic site catalysts on titania support.[20] Dong and co-workers, reported active and stable bifunctional plasma-induced defective TiO_{2-x} nanocatalysts that exhibits dramatically boosted electrocatalytic activity.[21] Surface defect engineering can also modulate the electronic structure of nanomaterials and induce new physicochemical properties, thus promoting their electrocatalytic performance for water splitting and CO_2 reduction applications. In titania oxygen vacancies (OVs), and Ti^{3+} defects are common. The oxygen vacancy can significantly affect the electric and optical properties by forming a donor level located at 1.8 eV below conduction band of titania. These defects are responsible for changes in the electronic conductivity and optical properties by providing mid gap states between the valence and conduction bands of titania.[22] Defects turn titania from semiconductor to metallic depending upon intensity of structural deformation. Due to oxygen vacancies (OVs), the corresponding titanium atoms are in close proximity and interact electrically, resulting in good conductivity.[23]

Defects can directly maximize the catalytic performance of nanocatalysts by improving the transport capacity of charge thereby triggering active reactions. In this regard researchers reported efficient electrocatalytic water splitting (*i.e.*, a low overpotential and small Tafel slope) by ultrathin 2D materials.[24] Also Ni based single atom catalyst (SAC) supported on GaN, MoS_2, Mo_2C, g-C_2N and graphyne monolayers[25] and single atom (SA)-functionalized graphitic carbon nitride (g-C_2N) monolayeretc emerged as promising electrocatalysts for CO_2 activation and reduction.[26–28] These defect structures with high-density active sites provide excellent conductivity, thus increasing the efficiency of various electrocatalysts.

In previous studies, defects have been introduced *via* different physical and chemical routes like proton implantation,[29] laser irradiation,[30] hydrogen plasma,[31] ionothermal treatment,[32] electrochemical oxidation,[33] electrochemical reduction,[34] nitrogen doping,[35] hydrogenation,[36] and chemical reduction using Al,[37] Mg,[38] $NaBH_4$,[39] CaH_2,[40] N_2H_2 [41] *etc*. Among these, physical methods tend to be more complex, requiring expensive equipment and resulting in lower defect concentrations which are undesirable in terms of improving intrinsic properties of titania. However, the reduction of high-valence state Ti from Ti^{4+} to Ti^{3+} or Ti^{2+} and the oxidization of low-valence state Ti from Ti^{2+} or Ti^{3+} to Ti^{4+} are reported to be effective chemical methods to induce high defect concentrations in Ti-based oxides.[42,43] In comparison with hydrogen, metal elements such as Li, Al, Mg and Zn possess relatively high reducing activities and can partially capture oxygen atoms to leave oxygen vacancies and Ti^{3+} centers in lattices.[37,44] Certain organic acids have also been used as modifier and structure directing agents for titania in order to achieve high surface area, porosity and narrow band gap.[17] But there is still lack of systematic investigation and discussion to study the effect of inorganic and organic reducing agents on catalytic properties of titania.

In the present study, visible light driven (VLD) reduced TiO_{2-x} is solvothermally synthesized using inorganic (Mg and Zn) and organic (L-ascorbic acid, citric acid) reducing agents. Acid treatment, in case of inorganic synthesis route further modifies the physicochemical properties of titania by increasing the surface area. The oxygen vacancies (OVs), low coordinated Ti ions (Ti^{3+}) and lattice-strained configuration of synthesized reduced TiO_{2-x} provide ample or sufficient active sites for electrochemical reactions (HER and OER) and extended photoresponse in visible region by modulating electrical conductivity and facilitating charge transfer kinetics, thus exhibiting better electrocatalytic and photocatalytic activities in comparison with pristine titania. Nevertheless, employing the co relational structural characterizations, such as XRD, XANES and quantitative EXAFS calculations, the local chemical environment and symmetry of reduced TiO_{2-x} were also deduced. This study offers a comprehension overview on the physicochemical properties, local atomic arrangements and electronic structures relationship of reduced TiO_{2-x} towards the OER, HER, and dye degradation. Accordingly, this work provides a valuable route to design high-performance, low-cost and non-precious metal oxide based multifunctional nanomaterials for photocatalysis and electrocatalytic overall water splitting.

2. Experimental

2.1. Synthesis of reduced TiO_{2-x} nanocatalysts

All reagents were purchased from Sigma-Aldrich and used without further purification. Reduced titania *via* inorganic routes (Zn and Mg) was synthesized according to a previously reported method with few modifications.[45] Typically, 3 mL of $TiCl_3$ (>12%) aqueous solution, Zn powder (0.3 g) and 90 mL of isopropanol were magnetically stirred for about 1.5 h. Then the solution mixture was poured into a 100 mL autoclave container (Teflon lined) and heated in a furnace at 180 °C for 6 h. The synthesized material was centrifuged and soaked in 4 M HCl aqueous solution (100 mL) for 1 h in order to remove un-reacted zinc powder. After washing with distilled water, the product was dried in oven at 80 °C to get nanocrystals of reduced titania *i.e.*, Zn–TiO_{2-x}. The same procedure was repeated with magnesium powder as an inorganic reducing agent in place of zinc powder to get reduced titania *i.e.*, Mg–TiO_{2-x} nanocatalysts.

2.2. Synthesis *via* organic route (L-ascorbic acid and citric acid)

Reduced titania nanocatalysts *via* organic route were synthesized following the reported method.[46] Typically, 0.6 g of L-ascorbic acid was magnetically stirred with 70 mL of distilled water for 15 min. The solution turned purple after the addition of 3 mL of $TiCl_3$ (>12%) aqueous solution. In order to raise pH up to 4, an appropriate amount of aqueous solution of NaOH (1 mol L^{-1}) was mixed to the solution. After 30 min stirring at room temperature, the solution was poured into a Teflon lined

stainless steel autoclave (100 mL) and placed in a furnace at 180 °C for 12 h. The obtained solid was washed and centrifuged with absolute ethanol. Finally, the product (abbreviated as AA–TiO_{2-x}) was dried overnight in oven at 80 °C. The same procedure was repeated with citric acid as an organic reducing agent in place of L-ascorbic acid to get product (abbreviated as CA–TiO_{2-x}) nanocatalysts.

The schematic synthesis of experimental details of EXAFS, electrochemical and photocatalytic dye degradation studies are given in ESI† S (i–iii) respectively.

2.3. Characterization

Powder X-ray diffraction (pXRD) spectra were collected using a PAN analytical X'Pert, employing Cu $K_{\alpha 1}$ radiation ($\lambda = 1.5418$) at 298 K. The N_2 adsorption/desorption measurements were performed by using a Quantachrome Nova 2200e. Prior to the measurement, samples were degassed under vacuum at 363 K overnight. Scanning electron microscope (SEM) images were obtained using a (FEI NOVA Nano SEM 450) equipped with energy-dispersive X-ray spectroscopy (EDX). EXAFS measurements were conducted at the Synchroton-Light for Experimental Science and Applications in the Middle East (SESAME) on the BM08-XAFS/XRF beamline. The ultraviolet-visible (UV-vis) absorption spectra of the nanocatalysts were measured using a PerkinElmer Lambda 35 UV-vis spectrophotometer, while the photoluminescence (steady state and time resolved) was studied using a Pico Quant Fluo Time-300 spectrophotometer. The photocurrent responses in the light on–off process were determined in a homemade three electrode quartz cell containing 0.1 mol L^{-1} NaOH aqueous solution under visible lights (>420 nm) irradiation using xenon lamp with electrochemical workstation (CHI 660D).

3. Results and discussion

The powdered X-ray diffraction (pXRD) was conducted to compare the series of reduced TiO_{2-x} samples with commercial titania, to explore the crystal structure and possible phase changes after reduction. The diffraction peaks in Fig. 1 were marked by letter A, R and B respectively for anatase, rutile and brookite phases of TiO_2. The peaks of all reduced TiO_{2-x} samples are matching well with the anatase phase (ICDD/PDF 21-1272).[47] As presented in Fig. 1, the spectral peaks at 2θ = 25.64°, 38.26°, 48.40°, 53.54°, 54.80° and 63.00° are respectively assigned to the (101), (004), (200), (105), (211) and (204) crystal planes of titania in anatase phase. In case of Zn–TiO_{2-x} and Mg–TiO_{2-x}, two additional peaks located at 2θ = 27.74° and 30.89° were assigned to the (110) and (121) crystal planes of rutile (ICDD/PDF 21-1276) and brookite (ICDD/PDF 29-1360) respectively.[48] The particle sizes were calculated from the Scherrer equation by using FWHM values of the dominant peaks in Fig. 1. The derived dimensions D were calculated as 54, 12, 10, 24 and 10 nm for C–TiO_2, Zn–TiO_{2-x}, Mg–TiO_{2-x}, AA–TiO_{2-x} and CA–TiO_{2-x} respectively. The broadened peaks of the R-TiO_{2-x} samples in comparison with commercial titania can be

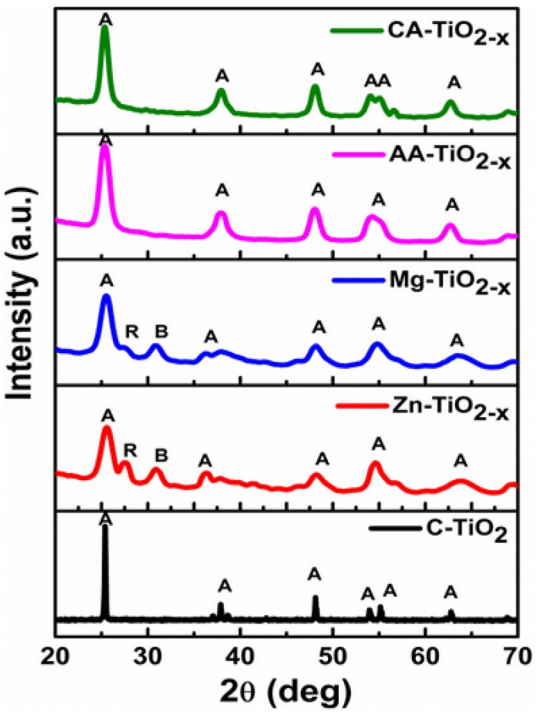

Fig. 1 XRD patterns of C–TiO_2, Zn–TiO_{2-x}, Mg–TiO_{2-x}, AA–TiO_{2-x} and CA–TiO_{2-x} nanocatalysts.

associated with the decrease in particle size and crystallinity of titania after reduction as reported earlier in literature.[49]

Raman spectroscopic technique was used to investigate all the nanomaterials. The Raman spectra of all samples showed six Raman active modes ($3E_g$ + $2B1_g$ + $A1_g$) of anatase TiO_2 (Fig. 2) which was consistent with XRD results and the previous work.[38,46] For anatase titania the three bands observed at 147, 198 and 640 cm^{-1} were associated to E_g mode while bands at 518 and 639 cm^{-1} were assigned to $A1_g$/$B1_g$ (un-resolved doublet) and $A1_g$ respectively. Out of these bands, the

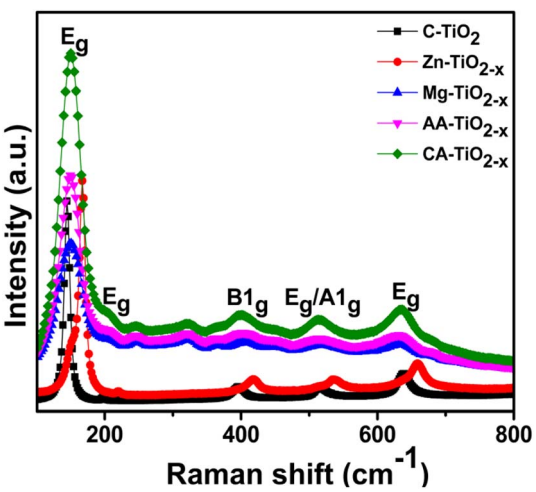

Fig. 2 Raman spectra of C–TiO_2, Zn–TiO_{2-x}, Mg–TiO_{2-x}, AA–TiO_{2-x} and CA–TiO_{2-x} nanocatalysts.

strongest band observed for anatase was at 147 cm^{-1}.[50] However, in comparison with the C–TiO_2 nanoparticles, it was observed in Fig. 2 that the frequency of the strongest E_g mode in reduced titania samples displayed a distinct blue shift. This peak originated from external vibration of the Ti–O bonds in titania. The reduced titania samples showed change in intensity and the position of Raman bands in comparison with the commercial titania. As reported earlier, these changes can be associated with the strain, non-stoichiometry, defects and anharmonic effects. In present case, it can be attributed that during reduction the octahedral symmetry of TiO_6 was destroyed on the surface of reduced titania. So, the observed band shifting by the synthesized nanocatalysts can be attributed to the presence of defects (OVs and Ti_{vac})[46] that was also confirmed by XAS, absorbance profile, band gap energies and photoluminescence (PL) spectra.

The Ti K-edge (4966 eV) X-ray absorption near edge structure (XANES) spectra of the commercial anatase titanium oxide (C–TiO_2) and all reduced titanium oxides, Mg–TiO_{2-x}, CA–TiO_{2-x}, AA–TiO_{2-x} and Zn–TiO_{2-x} are shown in Fig. S1.† These spectra displayed typical pre-edge peaks (P and Q) and above-edge features (R, S, T and U) of TiO_2 and the white line for all the materials. The features at the pre-edge regions are insensitive to Ti–O bond length, but are very sensitive to the Ti valence state.[51] The inset of Fig. 3, the commercial titania (C–TiO_2) showed all the three pre-edge features (P1, P2 and P3) that are characteristics of six-coordinated titanium (Ti_{6c}^{4+}) cations located in the anatase TiO_2 local structure (symmetry site). These peaks were formed due to the transfer of 1s core electron to the empty 3d valence states. The peak P1 was attributed to the quadruple transition of 1s electron to the t_{2g} states of octahedral TiO_6, whereas, peak P2 and P3 assignments were controversial. However, literature reported studies revealed that P2 was either assigned to the transition of 1s core electron to e_g states of octahedral TiO_6 or transition to the t_{2g} energy levels of neighboring octahedral.[52] The peak P3 was corresponded to the transition of 1s electron to the e_g states of neighboring Ti atoms or 4p states of absorbing atoms.[52]

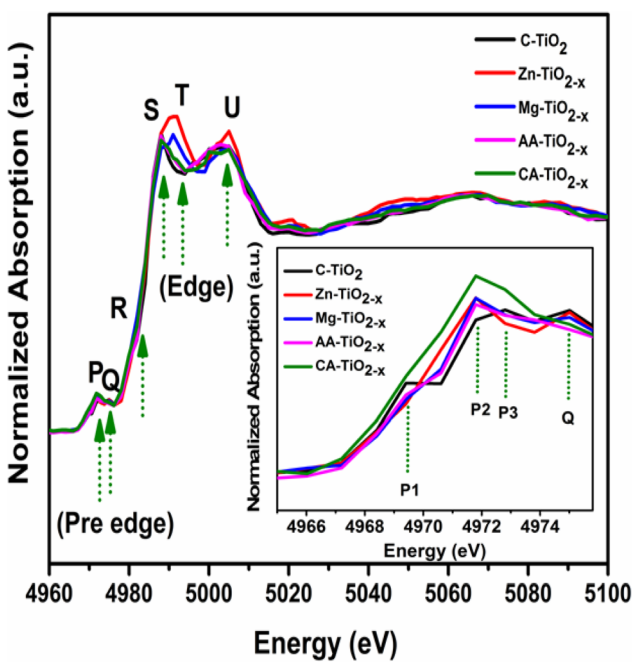

Fig. 3 XANES spectra of C–TiO_2, Zn–TiO_{2-x}, Mg–TiO_{2-x}, AA–TiO_{2-x} and CA–TiO_{2-x} nanocatalysts. The dotted vertical lines highlight the pre edge region (P and Q), and above the edge (R, S, T and U). The inset shows main pre-edge features of all nanomaterials (P1, P2, P3 and Q).

The observed increase in the intensity of the P2 peak for the Zn–TiO_{2-x}, Mg–TiO_{2-x} and AA–TiO_{2-x} reduced titania (Fig. 3) indicated distortion in TiO_6 octahedron or Ti-oxide (tetrahedral or pentahedral coordination) when compared to the commercial titania, which was more pronounced in CA–TiO_2. Moreover, for poorly crystalline TiO_2, a distorted or defective Ti local environment increased the resonance intensity at the pre-edge peak. These tetrahedral sites were believed to be created by d–p orbital mixing and gave evidence of the presence of five coordinated (Ti_{5c}^{4+}).[53] Though the pre-edge features was a result of 1s to 3d electron transitions (Laporte rules forbidden), however these transitions can be partially allowed by non-centrosymmetric orbital character and excited state.[51] The weak shoulder peak R was formed due to the 1s to 4p transition and white line peak S was ascribed to the transition of 1s core electron to higher-lying p atomic orbital. It was further identified that commercial titania exhibited well-resolved peaks and sharp features S and T at edge, due to its high crystallinity as indicated in XRD spectra (Fig. 1). On the other hand, the reduced TiO_2 materials displayed relatively broader and blurred S and T features due to the decreased crystallinity. The XANES spectrum of Zn–TiO_{2-x} appeared slightly different in near edge region when compared to other reduced titania due to the contribution from the rutile phase, corroborated by XRD pattern (Fig. 1).

The best fits to the Ti K-edge EXAFS of all the samples were performed in *R*-space from 1.0 to 3.6 Å intervals with Hanning window and in the *k* range of 2–11 $Å^{-1}$. The initial four shells of the Ti–$O_{eq./ax.}$ and Ti–Ti single scattering paths till 3.6 Å with high ranked multiple scattering paths were included in the best fit analysis. The amplitude reduction factor (S_0^2), and energy shift parameter (ΔE_0) were set similar for all the scattering paths. Whereas, the change in the half-path length (ΔR) and the mean-square relative displacement (σ^2) were refined relatively and the degeneracy of the O and Ti backscatterers (N) were varied accordingly with optimized minimum value of R_{factor} to explore the O vacancy and Ti vacancy in the lattice for the reduced titania, achieving the best fit result. The Fourier transforms of the EXAFS data (Fig. 4(a–d)) of commercial titania and reduced titania displayed the first major peak, attributed to the Ti–O coordination shells (Ti_0–$O_{eq.}$ and Ti–$O_{ax.}$). Whereas, the next peak appeared within the *R* range of 2–2.7 Å assigned to the first Ti_0–Ti_1 scattering path of anatase phase, as manifested in Fig. 4(a–d). The fit result manifested slightly lower number of degeneracy of the paths for first (Ti_0–$O_{eq.}$ = 3.8) and second (Ti–$O_{ax.}$ = 1.7) coordination shells of the commercial C–TiO_2 when compared to the standard anatase phase lattice (Ti_0–$O_{eq.}$ = 4 and Ti–$O_{ax.}$ = 2), suggesting slight distortion in the TiO_6 octahedron.

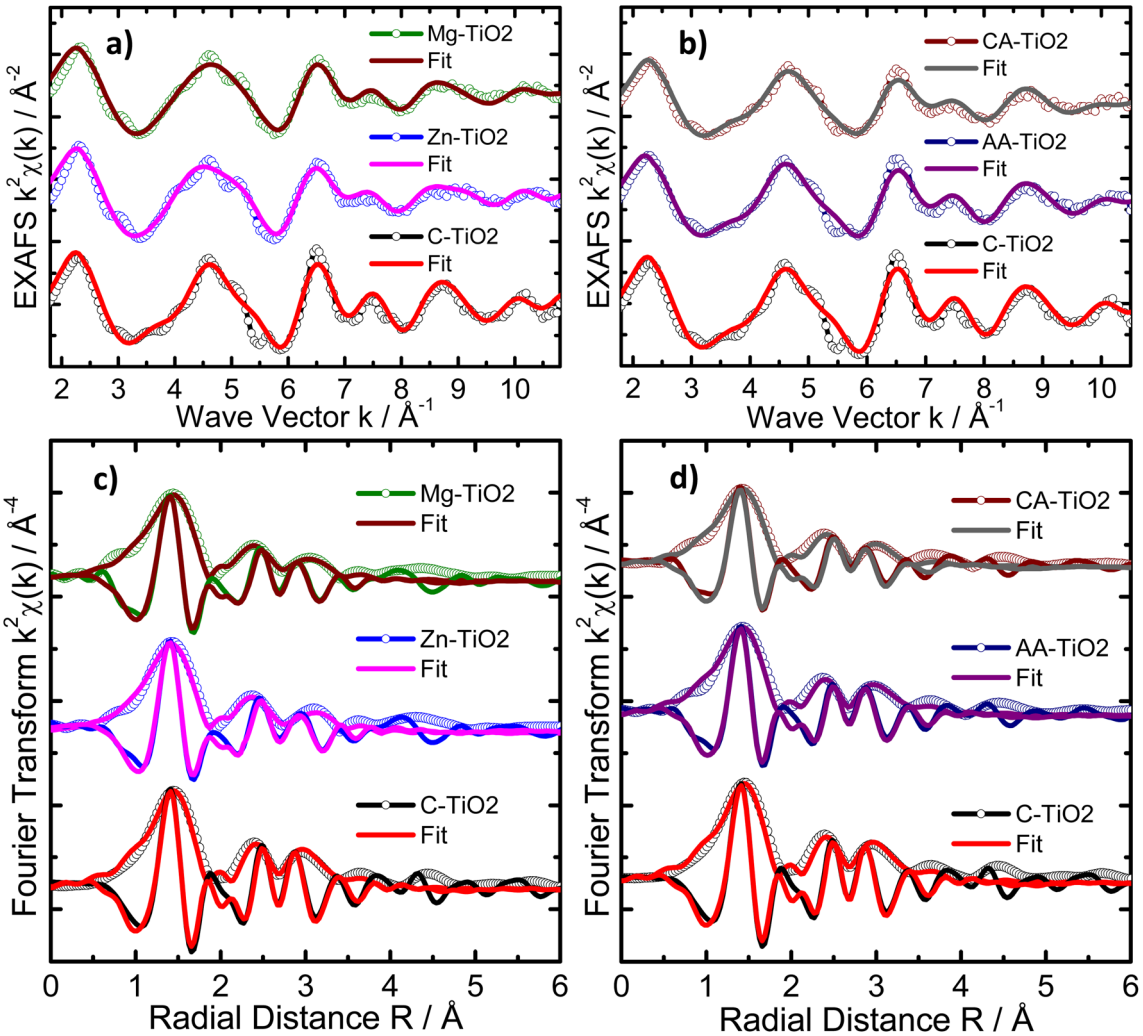

Fig. 4 The k^2-weighted EXAFS plots (top) and their Fourier transforms (bottom) with best fits at the Ti K-edge for C–TiO_2 and synthesized reduced TiO_{2-x}, including Zn–TiO_{2-x}, Mg–TiO_{2-x} (a and c), AA–TiO_{2-x} and CA–TiO_{2-x} (b and d), showing the amplitude and the real parts of the Fourier transforms of the data and the fits.

The AA–TiO_{2-x} nanomaterial exhibited a similar structure as the commercial titania (C–TiO_2), demonstrated by the approximately identical values of structural parameters (Table S1†), principally degeneracy of the paths (N) and Debye–Waller factor (σ^2). These results clearly indicated the existence of partial OVs in the first and second coordination shell (Ti_0–$O_{eq.} = 3.5$ and Ti–$O_{ax.} = 1.3$), suggesting distorted tetrahedral or pentahedral local chemical environment around the Ti for the CA–TiO_{2-x} nanomaterial (Table S1†) corroborated through the corresponding near edge structure (XANES) study. Nevertheless, the considerable lowering in the N values of fourth scattering paths (Ti_0–Ti_2) with higher values of Debye–Waller factor (σ^2) indicated the generation of Ti vacancy in fourth coordination shell at Ti_2 site of the lattice (Fig. 4(a and c)) with considerable structural disorder for the Zn–TiO_{2-x} and Mg–TiO_{2-x} nanomaterials. The 3D structure of anatase titania is presented in Fig. S2† where titanium atoms at the different positions along with the axial and equatorial oxygen atoms are also labeled.

Furthermore, SEM and EDX analyses further provided the details about the morphology and chemical composition of the as synthesized materials and commercial TiO_2. The SEM images of the commercial titania nanoparticles demonstrated an almost spherical shape as shown in Fig. S3(a and b).† However, compact and agglomerated morphology of all synthesized nanocatalysts as presented in SEM images (Fig. S3† displays SEM images of Zn–TiO_{2-x} (c and d), Mg–TiO_{2-x} (e and f), AA–TiO_{2-x} (g and h) and CA–TiO_{2-x} (i and j)) which can be due to particle size reduction. This compact morphology can be related to the broadened peaks of XRD in comparison with commercial titania which are in a line with particle size calculations. EDX measurement in Fig. S4(a–e)† confirmed that all the nanomaterials were composed of Ti and O elements, implying the absence of any impurity. These results are in a line with the XRD results Fig. 1.

The pore size distribution curves presented in Fig. 5(a) revealed the existence of all reduced TiO_{2-x} samples in mesopore range (2 nm < pore size < 50 nm). The size distribution

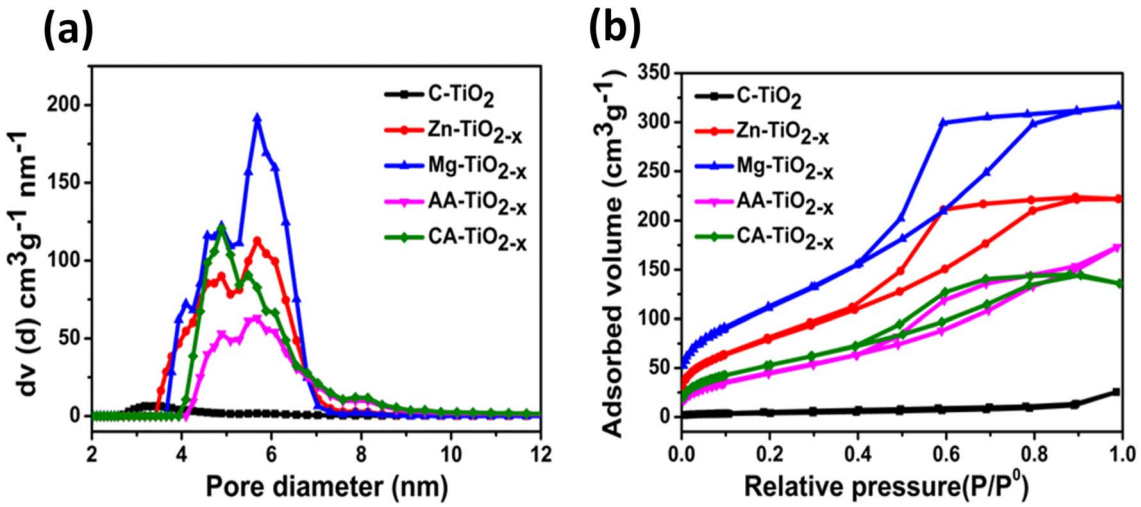

Fig. 5 (a) Pore size distribution plots of the nano-catalysts (b) N_2 adsorption–desorption isotherms of all the nanomaterials.

curves showed the presence of a pore diameter of the synthesized nanocatalysts in the range of 2–7 nm. The mesoporosity of the synthesized nanocatalysts are believed to promote the diffusion and transportation of the reactants from the aqueous phase to the inner and outer surface of the catalysts. The average pore diameters of the materials are tabulated in the Table S2.† The reduced titania synthesized *via* inorganic routes showed greater pore widths in comparison with other nanomaterials. The nitrogen adsorption–desorption isotherms of all samples are shown in Fig. 5(b).

All the R-TiO_{2-x} catalysts exhibited the type-IV isotherms with a clear hysteretic loop, suggesting the mesoporous features with high energy of adsorption (P/P^0).[54] More importantly, the reduced TiO_{2-x} synthesized *via* organic and inorganic routes showed the presence of different types of hysteresis loops. According to the classification (IUPAC), the Zn–R-TiO_{2-x} and Mg–R-TiO_{2-x} catalysts showed the isotherm of type IV with H2 hysteresis loops in the relative pressure (P/P^0) range of 0.41–0.9. Type IV isotherms are typical for mesoporous materials. The catalysts showing IV-type isotherm along with the H2 hysteresis loop are believed to possess the cylindrical channels or aggregates (blended) or agglomerates (non blended) of spherical particles[55] as observed in SEM images.

The isotherms of AA–R-TiO_{2-x} and CA–R-TiO_{2-x} catalysts were of type IV, having mesoporous structure with H4 hysteresis loop at a relative pressure (P/P^0) of 0.4–0.9. These features indicated that these nanomaterials possessed narrow slit pores and a broader inner part. The presence of organic acids significantly alter the surface area and pore structure of titania.[46] Table S2† shows the specific surface area (S_{BET}) of 247.925, 342.598, 145.654 and 228.254 $m^2\ g^{-1}$ with pore volume (V_p) of 0.335, 0.466, 0.228 and 0.332 $cm^3\ g^{-1}$ for Zn–TiO_{2-x}, Mg–TiO_{2-x}, AA–TiO_{2-x} and CA–TiO_{2-x} respectively. In comparison, the commercial titania possessed a barely measurable surface area of 14.243 $m^2\ g^{-1}$ and a pore volume of 0.020 $cm^3\ g^{-1}$. Out of all nanocatalysts, the Zn–R-TiO_{2-x} and Mg–R-TiO_{2-x} had greater surface area and pore volume resulting in availability of the more active sites for electrocatalytic water splitting. It has been postulated that the acidic conditions during the synthesis significantly enhanced the textural properties of titania.[56] It is evident from Table S2† that the reduced titania nanocatalysts synthesized *via* inorganic routes undergo acid treatment and possessed larger surface area values. The large surface area and mesoporous structure could enhance the water adsorption on the catalyst surface thereby facilitating the water splitting. Therefore, the synthesized mesoporous materials not only can enhance the photocatalysis by effective solar energy harvesting within the mesopores but also provide the surface active sites for water splitting.

The optical properties of all the R-TiO_{2-x} powdered samples and commercial titania were characterized by UV-visible spectroscopy. Fig. 6(a) illustrates the strong absorption exhibited by the commercial TiO_2 in ultraviolet region, while the synthesized reduced TiO_{2-x} samples display a broad absorption in the UV-vis region. This absorption band below 400 nm can be ascribed to the band gap excitation of anatase TiO_2 that arises due to the transition from 3d orbital of Ti to 2p orbital of O.[57] The band gap energies of commercial and the synthesized nanocatalysts were obtained from Kubelka–Munk function equation[58](Table S3†). The plots in Fig. 6(b) depicted the reduced band gap energy for reduced TiO_{2-x} nanomaterials *i.e.*, below 3 eV in comparison with commercial titania. The reduced titania samples also presented an extended absorption tail known as urbach which is associated with various defects. It is reported that the new band is created below the conduction band of titania due to the presence of large number of OVs.[59] The AA–TiO_{2-x} showed increase visible light absorption, much superior to the commercial anatase that reduced its band gap below 1.5 eV. Thus introduction of defects into the structure of titania augmented the visible light absorption.[60] This behavior was further compelled by the XAS data which showed the presence of the two different types of defects in the reduced titania samples.

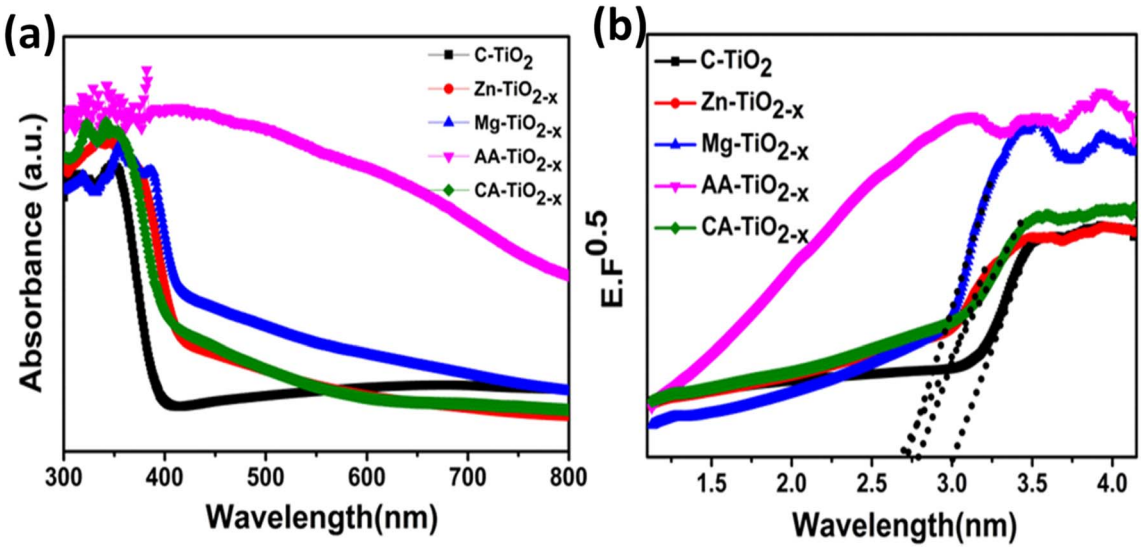

Fig. 6 (a) UV-visible plots of the photocatalysts (b) DRS spectra of different photocatalysts.

Conventional methods of PL have been used for decades to understand the properties of titania, specifically, information like the quality of the material, the specific origin and nature of the electronic transitions that can be obtained from PL spectra.[61] Generally, steady state photoluminescence (SSPL) spectrum of anatase titania represents three peaks having different type of physical origin *i.e.*, self-trapped excitons (STE), oxygen vacancies (OVs) and surface states.[62,63] From Fig. 7 it can be seen that the high intensity emission peak observed for all samples lies in the violet region at 418 nm (2.9 eV). This high intensity peak can be allocated to radiative recombination of STE for bulk TiO_2.[63] Furthermore, it is clear from Fig. 7 that all nanomaterials showed broader emission peak from 450 nm to 600 nm corresponding to the oxygen vacancy defects (green band located at 1.8–2.5 eV below the conduction band).[64] This peak aligns with the presence of oxygen vacancy defects, which is in line with results of UV-visible spectroscopy. The distinct PL peak centered at 525 nm was more prominent in case of the synthesized nanocatalysts. After defect formation, the PL intensity of reduced titania photocatalysts were quenched significantly. This quenching behavior can be related to the defect centers that ultimately facilitate the charge transfer mechanism during photocatalysis.[65]

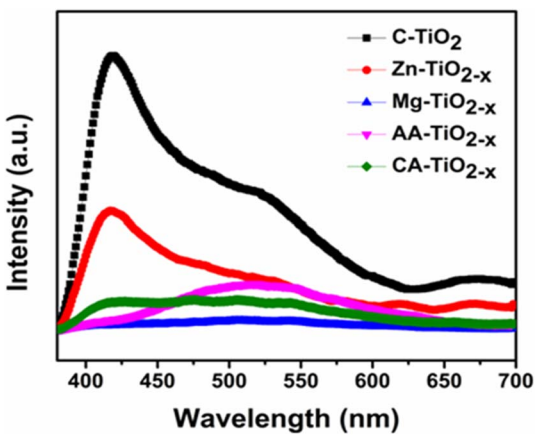

Fig. 7 Steady state photoluminescence (SSPL) plots of the C–TiO_2, Zn–TiO_{2-x}, Mg–TiO_{2-x}, AA–TiO_{2-x} and CA–TiO_{2-x} photocatalysts.

4. Electrochemical studies of nanocatalysts

The electrochemistry offers various practical and viable routes for water splitting.[66] LSV was employed to probe the electrocatalytic activity of all the synthesized nanocatalysts. The experiments were performed in 0.1 M NaOH at a scan rate of 50 mV s^{-1}. Fig. 8(a) shows a significant improvement in electrochemical activity upon the modification of commercial titania by using inorganic and organic reducing agents, as indicated by reduction in the onset potential. The Mg–TiO_{2-x} electrocatalyst found to be superior compared to other catalysts, with an OER over potential equal to 420 mV *vs.* RHE at current density of 10 mA cm^{-2}. All the R-TiO_{2-x} electrocatalysts showed smaller Tafel slope values Fig. 8(b) for OER in comparison with the unmodified titania. The synthesized materials offered OER overpotential <500 mV with smaller Tafel slopes in alkaline medium which are better than the reported porous Co_3O_4 nanoplates (523 mV, 71 mV dec^{-1})[67] and $NiCo_2O_4$ nano-needles (565 mV, 292 mV dec^{-1}).[68]

Similar trend was observed for the HER (Fig. 8(c)) by all the modified titania electrocatalysts. Compared with commercial titania all the synthesized nanomaterials displayed lower HER over potential. Xu Jijian *et al.* reported almost 5 times greater hydrogen production by magnesium reduced titania in comparison with the unmodified titania during the photoelectrochemical water splitting.[69] Similarly, Mg–TiO_{2-x} presented lowest HER overpotential *i.e.*, 650 mA cm^{-2}. Table S4† compares the over potentials and Tafel slopes of all the nanomaterials. The enhanced activity of reduced titania nanocatalysts is attributed to their increased surface area and the

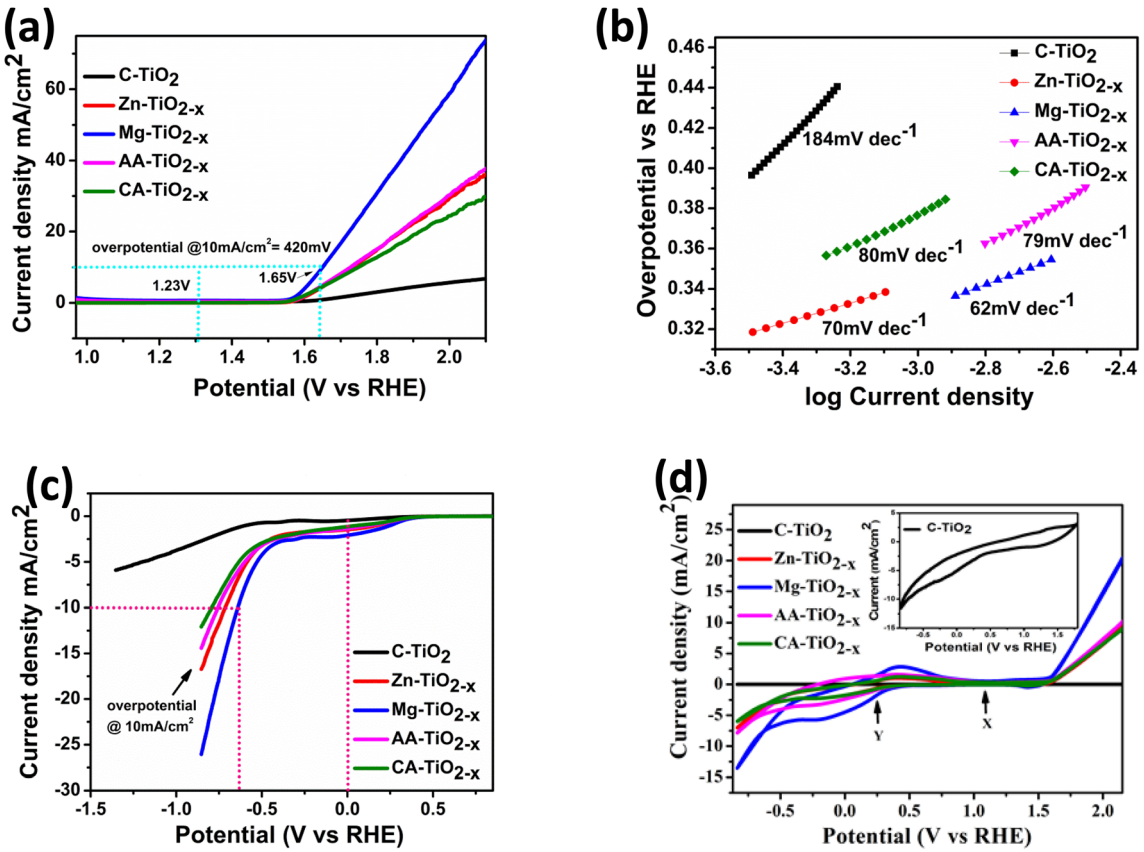

Fig. 8 (a) Linear sweep voltammetric (LSV) data of electrocatalysts for the OER, (b) comparison of Tafel plot for OER of electrocatalysts, (c) linear sweep voltammograms of electrocatalysts for HER and (d) cyclic voltammograms of prepared electrocatalysts and C–TiO_2 (inset).

presence of defects *i.e.*, oxygen vacancies and titanium vacancies.

Cyclic voltammetry (CV) was conducted on all the electrodes between −0.8 and +2.1 V *vs.* RHE at 50 mV s^{-1} scan rate (Fig. 8(d)) in alkaline medium. The shape of CV curves of all the reduced TiO_{2-x} electrodes was typical for titanium dioxide materials with a marginal capacitive in anodic region.[70] However, all the modified materials showed metal reduction peaks as the electrochemical reaction proceeded; there was a possibility of change in the electronic structure of titania after reducing into the lower oxidation states.[71] Thus the conductivity of R-TiO_{2-x} was enhanced in comparison with commercial titania, as the formation of additional energy levels within the band gap is believed to influence the electrical conductivity as well as the optical properties of the material.[72] Beyond the metal reduction peak, at more negative potential the hydrogen evolution process was initiated. When the potential was reversed the re-oxidation of the electrodes started. Finally, at more positive potential after 1.5 V the evolution of oxygen observed.

The basic concept behind the enhanced electrocatalytic activity of all the R-TiO_{2-x} nanomaterials is the presence of large surface area and mesoporous structure that provide abundant space for hydrogen and oxygen adsorption. More importantly, the enhancement in conductivity of R-TiO_{2-x} is related to the existence of defect sites (OVs and Ti_{vac}). The vacancies induce the perturbation resulting in vacancy channels *via* vacancy–vacancy, vacancy–strain coupling and vacancy–electron interaction.[13] Thus, the commercial TiO_2 showed decreased activity, due to its low conductivity and small surface area values.

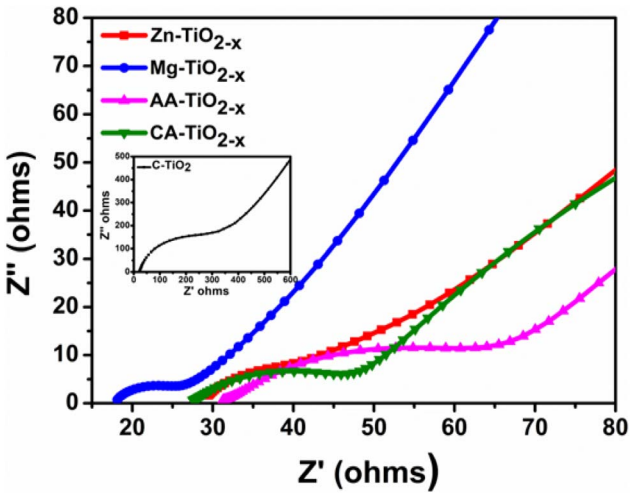

Fig. 9 Nyquist plot of the synthesized electrocatalysts and their comparison with C–TiO_2 (inset).

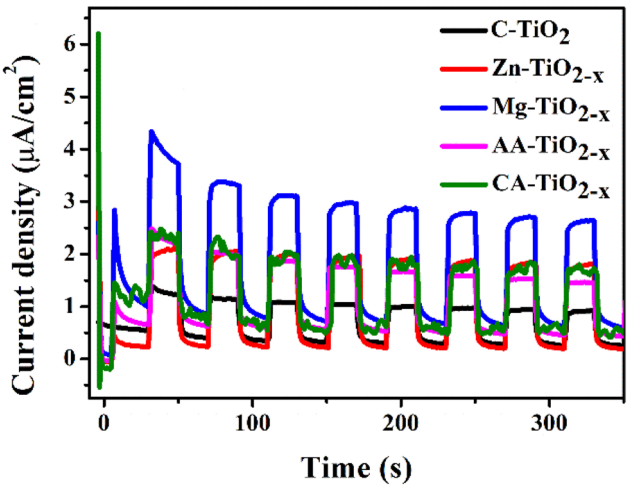

Fig. 10 Photoresponse of C–TiO_2, Zn–TiO_{2-x}, Mg–TiO_{2-x}, AA–TiO_{2-x} and CA–TiO_{2-x} photocatalysts.

Electrochemical impedance spectroscopy (EIS) is effective technique for the interpretation of phenomena such as electrocatalysis and corrosion. For analysis purposes, a model is applied to handle the data using equivalent circuits. These electrical circuits consist of different elements *e.g.*, constant phase element (CPE), resistors, inductors and Warburg elements.[73] This technique can provide insight into charge transport mechanism.[74] For all electrocatalysts the constant phase model (CPE) with diffusion was applied with equivalent circuit presented in Fig. S5.† The solution resistance (R_s), charge transfer resistance (R_{ct}), CPE and Warburg resistance (R_w) are the main parameters of this model. In order to provide additional evidence for the photocurrent response, the EIS was carried out in alkaline medium. In Fig. 9 the Nyquist plots (real Z *vs.* imaginary Z) of all the samples are shown, where the arc radius of these plots can be related directly to the charge transfer resistance.[75] It can be seen from the Fig. 9 that the arc radii of all the samples showed trend similar to the photocurrent response in Fig. 10. The commercial titania nanocatalyst showed a larger impedance with bigger arc (inset of Fig. 9) in comparison with reduced titania samples. Table S4† presents all the fitting parameters of electrocatalysts where the least charge transfer resistance was offered by the Mg–TiO_{2-x} electrocatalyst. Thus, with higher surface area Mg–TiO_{2-x} can effectively decrease the recombination, which in turn leads to the high photocurrent response and improved photocatalytic activity. It is obvious that charge transfer kinetics and the catalytic ability of titania have been improved by defect generation.

5. Photocatalytic studies of nanocatalysts

The transient photocurrent responses of the photocatalysts were recorded *via* several on–off cycles of irradiation and the results are presented in Fig. 10. In comparison with commercial titania, all R-TiO_{2-x} samples exhibited an increased photocurrent density. The photocurrent response was reasonably higher by magnesium reduced titania which is in accordance with literature[69] and could be attributed to highest surface area and the presence of defects in the structure. This improvement indicated the greater efficiency of charge carrier separation, which can be related to the optical, structural and textural modifications in titania after reduction. From the photocurrent measurements, it can be considered that the presence of defects and mesoporous structures minimized the electron–hole recombination while high surface area was favorable for the interfacial separation of charge carriers over longer time.

In order to investigate the photocatalytic performance, the absorbance changes of reactive blue (RB-866) dye solution was measured with all photocatalysts in the presence of sunlight.

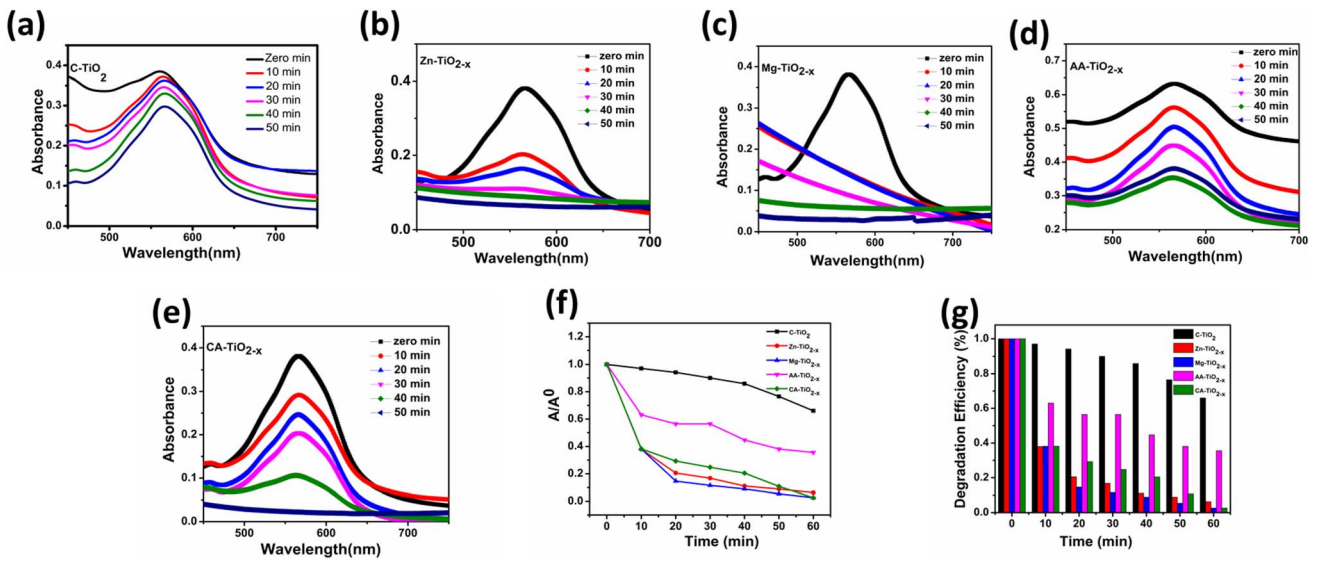

Fig. 11 (a–e) Change in absorbance of RB-866 as a function of irradiation time in the presence of photocatalysts, (f and g) change in concentration of RB-866 dye as a function of irradiation time in the presence of photocatalysts.

Degradation can be observed (Fig. 11(a–e)) as a decrease in absorbance maximum (λ_{max}) at 565 nm for the reactive blue dye. The Fig. 11(f and g) represents the degradation *versus* time in the presence of photocatalysts. It is believed that photocatalytic activity depends on the structural, optical and surface properties of a photocatalyst.[76] Among all, the Mg–TiO_{2-x} and Zn–TiO_{2-x} photocatalyst indicated superior photocatalytic activity which is consistent with TRPL, photoresponse and EIS results.

In the present study, the enhanced activity by the reduced titania photocatalysts can be ascribed to the increased optical absorption by defects, which facilitates the separation of photo-induced charge carriers. More importantly, the (OVs) in the reduced titania enhanced the visible light response thereby the generation of abundant electron–hole pairs, which were ultimately converted into active ions ($^{\bullet}O^{2-}$ and $^{\bullet}OH$) to decompose the dye molecules. These results are similar to the magnesium doped titania catalysts that showed better photodegradation of methyl orange dye in the presence of visible light.[77] Moreover, the mesoporous materials are suitable for photocatalysis because of the presence of numerous porous passages,[46] as large surface area and rich pore structure of R-TiO_{2-x} increased the probability of collision of dye molecules and the adsorbed active species on the catalyst surface. It is believed that the photocatalysis occurs on the illuminated surface, so smaller crystallite size and larger surface area results in fast transfer of adsorbed species from bulk onto the catalyst surface, causing the efficient photocatalytic activity.[75]

6. Conclusions

In present study mesoporous reduced TiO_{2-x} nanomaterials have been solvothermally synthesized using inorganic and organic reducing agents. SEM micrographs of synthesized nanocatalysts show compact morphology with little agglomeration. The reduced TiO_{2-x} samples show broad absorption in the UV-visible region with the band gap reduction. The enhanced textural, optical and electro-conducting properties of reduced TiO_{2-x} ensure superior photocatalytic activity and ultrafast kinetics of HER and OER. The defects and large surface area of reduced TiO_{2-x} significantly increase the visible light absorption, facilitating the charge carrier separation. The reduced TiO_{2-x} obtained *via* inorganic synthesis route are found to give superior electrocatalytic and photocatalytic response. In comparison to other catalysts, the Mg–TiO_{2-x} electrocatalyst stands out as superior, with an over potential of 420 mV *vs.* RHE for the oxygen evolution reaction (OER) at a current density of 10 mA cm^{-2}. Thus the synthesized reduced TiO_{2-x} nanomaterials are found to be efficient multifunctional heterogeneous catalysts for oxygen evolution, hydrogen evolution and dye degradation reactions.

Author contributions

Sadaf Jamil: methodology, conceptualization, formal analysis, writing – original draft. Naila Jabeen: conceptualization, supervision, resources, validation, review & editing. Fatima Sajid: writing – original draft, review & editing, formal analysis. Latif U. Khan: data curation, formal analysis, software & writing. Afia Kanwal: formal analysis. Manzar Sohail: data curation. Muhammad Zaheer: formal analysis. Zareen Akhter: supervision, resources, project administration, validation, visualization, writing – review & editing.

Conflicts of interest

The authors declare that they have no known competing financial interests or personal relationships that could have appeared to influence the work reported in this paper.

Acknowledgements

The authors acknowledge the Latif Ullah Khan (Beamline Scientist), BM-08 XAFS/XRF beamline of SESAME synchrotron light source for XAFS data measurement (Proposal No. 20190191).

References

1 H. Dau, C. Limberg, T. Reier, M. Risch, S. Roggan and P. Strasser, The mechanism of water oxidation: from electrolysis *via* homogeneous to biological catalysis, *ChemCatChem*, 2010, **2**, 724–761.
2 E. Fabbri, A. Habereder, K. Waltar, R. Kötz and T. J. Schmidt, Developments and perspectives of oxide-based catalysts for the oxygen evolution reaction, *Catal. Sci. Technol.*, 2014, **4**, 3800–3821.
3 A. Khataee and G. A. Mansoori, *Nanostructured Titanium Dioxide Materials: Properties, Preparation and Applications*, World scientific, 2011.
4 X. Chen, S. Shen, L. Guo and S. S. Mao, Semiconductor-based photocatalytic hydrogen generation, *Chem. Rev.*, 2010, **110**, 6503–6570.
5 M. A. Fox and M. T. Dulay, Heterogeneous photocatalysis, *Chem. Rev.*, 1993, **93**, 341–357.
6 A. Fujisima and K. Honda, Photolysis-decomposition of water at surface of an irradiated semiconduction, *Nature*, 1972, **238**, 37–38.
7 K. Raj and B. Viswanathan, Effect of surface area, pore volume and particle size of P25 titania on the phase transformation of anatase to rutile, *Indian J. Chem.*, 2009, 1378–1382.
8 Z. W. Seh, J. Kibsgaard, C. F. Dickens, I. B. Chorkendorff, J. K. Nørskov and T. F. Jaramillo, Combining theory and experiment in electrocatalysis: Insights into materials design, *Science*, 2017, **355**(6321), eaad4998.
9 D. Strmcnik, P. P. Lopes, B. Genorio, V. R. Stamenkovic and N. M. Markovic, Design principles for hydrogen evolution reaction catalyst materials, *Nano Energy*, 2016, **29**, 29–36.
10 J. Yao, H. Chen, F. Jiang, Z. Jiao and M. Jin, Titanium dioxide and cadmium sulfide co-sensitized graphitic carbon nitride nanosheets composite photocatalysts with superior performance in phenol degradation under visible-light irradiation, *J. Colloid Interface Sci.*, 2017, **490**, 154–162.

11 D. B. Hamal and K. J. Klabunde, Synthesis, characterization, and visible light activity of new nanoparticle photocatalysts based on silver, carbon, and sulfur-doped TiO_2, *J. Colloid Interface Sci.*, 2007, **311**, 514–522.

12 F. Wang, Y. Jiang, A. Gautam, Y. Li and R. Amal, Exploring the origin of enhanced activity and reaction pathway for photocatalytic H_2 production on Au/B-TiO_2 catalysts, *ACS Catal.*, 2014, **4**, 1451–1457.

13 J. Swaminathan, R. Subbiah and V. Singaram, Defect-Rich Metallic Titania ($TiO_{1.23}$) – An Efficient Hydrogen Evolution Catalyst for Electrochemical Water Splitting, *ACS Catal.*, 2016, **6**, 2222–2229.

14 A. M. Czoska, S. Livraghi, M. Chiesa, E. Giamello, S. Agnoli, G. Granozzi, E. Finazzi, C. Di Valentin and G. Pacchioni, The nature of defects in fluorine-doped TiO_2, *J. Phys. Chem. C*, 2008, **112**, 8951–8956.

15 L. Kong, C. Wang, H. Zheng, X. Zhang and Y. Liu, Defect-induced yellow color in Nb-doped TiO_2 and its impact on visible-light photocatalysis, *J. Phys. Chem. C*, 2015, **119**, 16623–16632.

16 Y.-K. Peng, Y. Hu, H.-L. Chou, Y. Fu, I. F. Teixeira, L. Zhang, H. He and S. C. E. Tsang, Mapping surface-modified titania nanoparticles with implications for activity and facet control, *Nat. Commun.*, 2017, **8**, 1–13.

17 M. Marszewski, J. Marszewska, S. Pylypenko and M. Jaroniec, Synthesis of porous crystalline doped titania photocatalysts using modified precursor strategy, *Chem. Mater.*, 2016, **28**, 7878–7888.

18 Z. Su, J. Liu, M. Li, Y. Zhu, S. Qian, M. Weng, J. Zheng, Y. Zhong, F. Pan and S. Zhang, Defect engineering in titanium-based oxides for electrochemical energy storage devices, *Electrochem. Energy Rev.*, 2020, 1–58.

19 A. Chalgin, W. Chen, Q. Xiang, Y. Wu, F. Li, F. Shi, C. Song, P. Tao, W. Shang and J. Wu, Manipulation of Electron Transfer between Pd and TiO_2 for Improved Electrocatalytic Hydrogen Evolution Reaction Performance, *ACS Appl. Mater. Interfaces*, 2020, **12**, 27037–27044.

20 M. Shahrezaei, S. M. H. Hejazi, H. Kmentova, V. Sedajova, R. Zboril, A. Naldoni and S. Kment, Ultrasound-Driven Defect Engineering in TiO_{2-x} Nanotubes – Toward Highly Efficient Platinum Single Atom- Enhanced Photocatalytic Water Splitting, *ACS Appl. Mater. Interfaces*, 2023, **15**, 37976–37985.

21 K. Dong, J. Liang, Q. Li, D. Ma, K. Dong, J. Liang, Y. Wang, Y. Ren, Z. Xu, H. Zhou and L. Li, Article Plasma-induced defective TiO_{2-x} with oxygen vacancies: A high-active and robust bifunctional catalyst toward H_2O_2 electrosynthesis Plasma-induced defective TiO_{2-x} with oxygen vacancies: A high-active and robust bifunctional catalyst toward, *Chem Catal.*, 2021, **1**, 1437–1448.

22 L. Andronic and A. Enesca, Black TiO_2 Synthesis by Chemical Reduction Methods for Photocatalysis Applications, *Front. Chem.*, 2020, **8**, 1–8.

23 S. Jayashree and M. Ashokkumar, Switchable intrinsic defect chemistry of titania for catalytic applications, *Catalysts*, 2018, **8**, 1–25.

24 Y. S. Cho, Two-dimensional materials as catalysts, interfaces, and electrodes for an efficient hydrogen evolution reaction, *Nanoscale*, 2024, **16**, 3936–3950.

25 R. Khanam, A. Hassan, Z. Nazir and M. A. Dar, Nickel single atom catalyst supported on the gallium nitride monolayer: first principles electrocatalytic reduction of CO_2, *Sustainable Energy Fuels*, 2023, **7**, 5046–5056.

26 M. A. Dar, Implications of the Pore Size of Graphitic Carbon Nitride Monolayers on the Selectivity of Dual-Boron Atom Catalysts for the Reduction of N_2 to Urea and Ammonia: A Computational Investigation, *Inorg. Chem.*, 2023, **62**, 13672–13679.

27 M. S. Functionalization, S. Fozia, A. Hassan, S. A. Reshi, P. Singh, G. A. Bhat, M. Dixit and M. A. Dar, Boosting CO_2 Activation and Reduction by Engineering the Electronic Structure of Graphitic Carbon Nitride through Transition, *J. Phys. Chem. C*, 2023, **127**, 11911–11920.

28 M. Zafari, A. S. Nissimagoudar, M. Umer and G. Lee, First principles and machine learning based superior catalytic activities and selectivities for N_2, *J. Mater. Chem. A*, 2021, **9**, 9203–9213.

29 N. Liu, V. Häublein, X. Zhou, U. Venkatesan, M. Hartmann, M. Mačković, T. Nakajima, E. Spiecker, A. Osvet and L. Frey, "Black" TiO_2 nanotubes formed by high-energy proton implantation show noble-metal-co-catalyst free photocatalytic H_2-evolution, *Nano Lett.*, 2015, **15**, 6815–6820.

30 X. Chen, D. Zhao, K. Liu, C. Wang, L. Liu, B. Li, Z. Zhang and D. Shen, Laser-modified black titanium oxide nanospheres and their photocatalytic activities under visible light, *ACS Appl. Mater. Interfaces*, 2015, **7**, 16070–16077.

31 X. Chen, L. Liu, Z. Liu, M. A. Marcus, W.-C. Wang, N. A. Oyler, M. E. Grass, B. Mao, P.-A. Glans and Y. Y. Peter, Properties of disorder-engineered black titanium dioxide nanoparticles through hydrogenation, *Sci. Rep.*, 2013, **3**, 1–7.

32 G. Li, Z. Lian, X. Li, Y. Xu, W. Wang, D. Zhang, F. Tian and H. Li, Ionothermal synthesis of black Ti^{3+}-doped single-crystal TiO_2 as an active photocatalyst for pollutant degradation and H_2 generation, *J. Mater. Chem. A*, 2015, **3**, 3748–3756.

33 L. R. Grabstanowicz, S. Gao, T. Li, R. M. Rickard, T. Rajh, D.-J. Liu and T. Xu, Facile oxidative conversion of TiH_2 to high-concentration Ti^{3+}-self-doped rutile TiO_2 with visible-light photoactivity, *Inorg. Chem.*, 2013, **52**, 3884–3890.

34 C. Xu, Y. Song, L. Lu, C. Cheng, D. Liu, X. Fang, X. Chen, X. Zhu and D. Li, Electrochemically hydrogenated TiO_2 nanotubes with improved photoelectrochemical water splitting performance, *Nanoscale Res. Lett.*, 2013, **8**, 1–7.

35 S. Wei, R. Wu, J. Jian, F. Chen and Y. Sun, Black and yellow anatase titania formed by (H, N)-doping: strong visible-light absorption and enhanced visible-light photocatalysis, *Dalton Trans.*, 2015, **44**, 1534–1538.

36 G. Wang, H. Wang, Y. Ling, Y. Tang, X. Yang, R. C. Fitzmorris, C. Wang, J. Z. Zhang and Y. Li, Hydrogen-treated TiO_2 nanowire arrays for photoelectrochemical water splitting, *Nano Lett.*, 2011, **11**, 3026–3033.

37 C. Yang, Z. Wang, T. Lin, H. Yin, X. Lü, D. Wan, T. Xu, C. Zheng, J. Lin and F. Huang, Core–shell nanostructured "black" rutile titania as excellent catalyst for hydrogen production enhanced by sulfur doping, *J. Am. Chem. Soc.*, 2013, **135**, 17831–17838.

38 M. Ye, J. Jia, Z. Wu, C. Qian, R. Chen, P. G. O'Brien, W. Sun, Y. Dong and G. A. Ozin, Synthesis of black TiO_x nanoparticles by Mg reduction of TiO_2 nanocrystals and their application for solar water evaporation, *Adv. Energy Mater.*, 2017, **7**, 1601811.

39 D. Ariyanti, L. Mills, J. Dong, Y. Yao and W. Gao, $NaBH_4$ modified TiO_2: Defect site enhancement related to its photocatalytic activity, *Mater. Chem. Phys.*, 2017, **199**, 571–576.

40 S. Tominaka, Y. Tsujimoto, Y. Matsushita and K. Yamaura, Synthesis of nanostructured reduced titanium oxide: crystal structure transformation maintaining nanomorphology, *Angew. Chem.*, 2011, **123**, 7556–7559.

41 C. Mao, F. Zuo, Y. Hou, X. Bu and P. Feng, In situ preparation of a Ti^{3+} self-doped TiO_2 film with enhanced activity as photoanode by N_2H_4 reduction, *Angew. Chem.*, 2014, **126**, 10653–10657.

42 X. Chen, L. Liu, Y. Y. Peter and S. S. Mao, Increasing solar absorption for photocatalysis with black hydrogenated titanium dioxide nanocrystals, *Science*, 2011, **331**, 746–750.

43 X. Xin, T. Xu, J. Yin, L. Wang and C. Wang, Management on the location and concentration of Ti^{3+} in anatase TiO_2 for defects-induced visible-light photocatalysis, *Appl. Catal., B*, 2015, **176**, 354–362.

44 T. Lin, C. Yang, Z. Wang, H. Yin, X. Lü, F. Huang, J. Lin, X. Xie and M. Jiang, Effective nonmetal incorporation in black titania with enhanced solar energy utilization, *Energy Environ. Sci.*, 2014, **7**, 967–972.

45 Z. Zhao, H. Tan, H. Zhao, Y. Lv, L.-J. Zhou, Y. Song and Z. Sun, Reduced TiO_2 rutile nanorods with well-defined facets and their visible-light photocatalytic activity, *Chem. Commun.*, 2014, **50**, 2755–2757.

46 M. W. Shah, Y. Zhu, X. Fan, J. Zhao, Y. Li, S. Asim and C. Wang, Facile synthesis of defective TiO_{2-x} nanocrystals with high surface area and tailoring bandgap for visible-light photocatalysis, *Sci. Rep.*, 2015, **5**, 15804.

47 A. Bashir, F. Bashir, Z. Mehmood, M. S. Satti and Z. Akhter, Synthesis, characterisation and investigation of enhanced photocatalytic activity of Sm^{3+}, Ni^{2+} co-doped TiO_2 nanoparticles on the degradation of azo dyes in visible region, *Int. J. Nanopart.*, 2019, **11**, 37–61.

48 S. Pigeot-Rémy, D. Gregori, R. Hazime, A. Hérissan, C. Guillard, C. Ferronato, S. Cassaignon, C. Colbeau-Justin and O. Durupthy, Size and shape effect on the photocatalytic efficiency of TiO_2 brookite, *J. Mater. Sci.*, 2019, **54**, 1213–1225.

49 J. Xu, Z. Tian, G. Yin, T. Lin and F. Huang, Controllable reduced black titania with enhanced photoelectrochemical water splitting performance, *Dalton Trans.*, 2017, **46**, 1047–1051.

50 H. Richter, Z. P. Wang and L. Ley, The one phonon Raman spectrum in microcrystalline silicon, *Solid State Commun.*, 1981, **39**, 625–629.

51 G. A. Waychunas, Synchrotron radiation XANES spectroscopy of Ti in minerals; effects of Ti bonding distances, Ti valence, and site geometry on absorption edge structure, *Am. Mineral.*, 1987, **72**, 89–101.

52 M. Chergui, Charge Carrier and Phonon Dynamics in Transition Metal Oxide and in Lead-Halide Perovskite Nanoparticles, in *Proceedings of the nanoGe Fall Meeting 2018*, 2018, DOI: 10.29363/nanoge.fallmeeting.2018.265.

53 M. Fernández-García, C. Belver, J. C. Hanson, X. Wang and J. A. Rodriguez, Anatase-TiO_2 nanomaterials: Analysis of key parameters controlling crystallization, *J. Am. Chem. Soc.*, 2007, **129**, 13604–13612.

54 M. Thommes, K. Kaneko, A. V. Neimark, J. P. Olivier, F. Rodriguez-Reinoso, J. Rouquerol and K. S. W. Sing, Physisorption of Gases, with Special Reference to the Evaluation of Surface Area and Pore Size Distribution (IUPAC Technical Report), *Pure Appl. Chem.*, 2015, **87**(9–10), 1051–1069.

55 J. Feng, Q. Wang, D. Fan, L. Ma, D. Jiang, J. Xie and J. Zhu, Nickel-Based Xerogel Catalysts: Synthesis *via* Fast Sol–Gel Method and Application in Catalytic Hydrogenation of p-Nitrophenol to p-Aminophenol, *Appl. Surf. Sci.*, 2016, **382**, 135–143.

56 J. Zhou, B. Song, G. Zhao and G. Han, Effects of Acid on the Microstructures and Properties of Three-Dimensional TiO_2 Hierarchical Structures by Solvothermal Method, *Nanoscale Res. Lett.*, 2012, **7**(1), 1–10.

57 L. G. Devi, N. Kottam, B. N. Murthy and S. G. Kumar, Enhanced Photocatalytic Activity of Transition Metal Ions Mn^{2+}, Ni^{2+} and Zn^{2+} Doped Polycrystalline Titania for the Degradation of Aniline Blue under UV/Solar Light, *J. Mol. Catal. A: Chem.*, 2010, **328**(1–2), 44–52.

58 B. Choudhury and A. Choudhury, Oxygen defect dependent variation of band gap, Urbach energy and luminescence property of anatase, anatase–rutile mixed phase and of rutile phases of TiO_2 nanoparticles, *Phys. E*, 2014, **56**, 364–371.

59 J. Nowotny, T. Bak, M. K. Nowotny and L. R. Sheppard, TiO_2 Surface Active Sites for Water Splitting, *J. Phys. Chem. B*, 2006, **110**(37), 18492–18495.

60 M. Salari, S. H. Aboutalebi, A. Aghassi, P. Wagner, A. J. Mozer and G. G. Wallace, Disorder engineering of undoped TiO_2 nanotube arrays for highly efficient solar-driven oxygen evolution, *Phys. Chem. Chem. Phys.*, 2015, **17**, 5642–5649.

61 S. Paul and A. Choudhury, Investigation of the Optical Property and Photocatalytic Activity of Mixed Phase Nanocrystalline Titania, *Appl. Nanosci.*, 2014, **4**(7), 839–847.

62 Y. Lei and L. D. Zhang, Fabrication, characterization, and photoluminescence properties of highly ordered TiO_2 nanowire arrays, *J. Mater. Res.*, 2001, **16**, 1138–1144.

63 N. D. Abazović, M. I. Čomor, M. D. Dramićanin, D. J. Jovanović, S. P. Ahrenkiel and J. M. Nedeljković, Photoluminescence of anatase and rutile TiO_2 particles, *J. Phys. Chem. B*, 2006, **110**, 25366–25370.

64 K. Das, S. N. Sharma, M. Kumar and S. K. De, Morphology Dependent Luminescence Properties of Co Doped TiO_2 Nanostructures, *J. Phys. Chem. C*, 2009, **113**(33), 14783–14792.

65 J. Lee, X. Liu, A. Kumar, Y. Hwang, E. Lee, J. Yu, Y. D. Kim and H. Lee, Phase-Selective Active Sites on Ordered/Disordered Titanium Dioxide Enable Exceptional Photocatalytic Ammonia Synthesis, *Chem. Sci.*, 2021, **12**, 9619–9629.

66 S. Dunn, Hydrogen Futures: Toward a Sustainable Energy System, *Int. J. Hydrogen Energy*, 2002, **27**(3), 235–264.

67 X. Zhou, Z. Xia, Z. Tian, Y. Ma and Y. Qu, Ultrathin Porous Co_3O_4 Nanoplates as Highly Efficient Oxygen Evolution Catalysts, *J. Mater. Chem. A*, 2015, **3**(15), 8107–8114.

68 H. Shi and G. Zhao, Water Oxidation on Spinel $NiCo_2O_4$ Nanoneedles Anode: Microstructures, Specific Surface Character, and the Enhanced Electrocatalytic Performance, *J. Phys. Chem. C*, 2014, **118**(45), 25939–25946.

69 J. Xu, Z. Tian, G. Yin, T. Lin and F. Huang, Controllable Reduced Black Titania with Enhanced Photoelectrochemical Water Splitting Performance, *Dalton Trans.*, 2017, **46**(4), 1047–1051.

70 H. Du, Y. Xie, C. Xia, W. Wang and F. Tian, Electrochemical Capacitance of Polypyrrole–Titanium Nitride and Polypyrrole–Titania Nanotube Hybrids, *New J. Chem.*, 2014, **38**(3), 1284–1293.

71 H. Pelouchova, P. Janda, J. Weber and L. Kavan, Charge Transfer Reductive Doping of Single Crystal TiO_2 Anatase, *J. Electroanal. Chem.*, 2004, **566**(1), 73–83.

72 J. M. Macak, H. Tsuchiya, A. Ghicov, K. Yasuda, R. Hahn, S. Bauer and P. Schmuki, TiO_2 Nanotubes: Self-Organized Electrochemical Formation, Properties and Applications, *Curr. Opin. Solid State Mater. Sci.*, 2007, **11**(1–2), 3–18.

73 E. Barsoukov and J. R. Macdonald, *Impedance Spectroscopy: Theory, Experiment, and Applications*, John Wiley & Sons, 2018.

74 J. Li, G. Zhan, Y. Yu and L. Zhang, Superior Visible Light Hydrogen Evolution of Janus Bilayer Junctions *via* Atomic-Level Charge Flow Steering, *Nat. Commun.*, 2016, **7**(1), 1–9.

75 D. Zhang and L. Gao, Synthesis, Characterization and Excellent Photocatalytic Performance of Iron-Carbon-Codoped Mesoporous Titania Nanocrystallines, *Acta Phys. Pol., A*, 2018, **133**(5), 1150–1159.

76 D. Jiang, Y. Xu, D. Wu and Y. Sun, Visible-Light Responsive Dye-Modified TiO_2 Photocatalyst, *J. Solid State Chem.*, 2008, **181**(3), 593–602.

77 B. K. Avasarala, S. R. Tirukkovalluri and S. Bojja, Photocatalytic Degradation of Monocrotophos Pesticide—an Endocrine Disruptor by Magnesium Doped Titania, *J. Hazard. Mater.*, 2011, **186**(2–3), 1234–1240.